Sustainable Energy & Fuels

ROYAL SOCIETY OF CHEMISTRY

PAPER

View Article Online
View Journal | View Issue



Cite this: *Sustainable Energy Fuels*, 2024, **8**, 3182

# Improving the photoelectrocatalytic efficiency of $CuWO_4$ through molybdenum for tungsten substitution and coupling with $BiVO_4$†

Annalisa Polo, [a] Maria Vittoria Dozzi, *[a] Gianluigi Marra,[b] Kevin Sivula [c] and Elena Selli [a]

A systematic investigation on the photoelectrocatalytic (PEC) performance of a series of $CuW_{1-x}Mo_xO_4$ materials with different Mo for W substitution ($x$ = 0–0.8), successfully synthesized as single, transparent photoactive layers, allowed us to identify copper molybdo-tungstate with $x$ = 0.5 ($CuW_{0.5}Mo_{0.5}O_4$) as the best performing Mo-containing $CuWO_4$-based material for photoanodes fabrication. For 250 nm thick material, the $CuW_{0.5}Mo_{0.5}O_4$ exhibits a 6-fold photocurrent increase at 1.23 V *vs.* RHE with respect to pure $CuWO_4$. Both PEC analyses in the presence of $NaNO_2$ as sacrificial agent and intensity modulated photocurrent spectroscopy (IMPS) measurements, here applied to this class of materials for the first time, demonstrate that the superior PEC performance of $CuW_{0.5}Mo_{0.5}O_4$ stems from a more efficient separation of photoproduced charges with respect to $CuWO_4$, while the charge injection efficiency is close to 100% for both materials. Further enhanced separation of photoproduced charges, resulting in increased PEC performance of the $CuW_{0.5}Mo_{0.5}O_4$ electrode in the 400–480 nm wavelength range, can be achieved by coupling it with $BiVO_4$, to form a type II heterojunction system.

Received 30th January 2024
Accepted 13th June 2024

DOI: 10.1039/d4se00161c

rsc.li/sustainable-energy



## 1. Introduction

The efficient harnessing of the inexhaustible energy that is freely available from the Sun, capable of delivering to the Earth in one hour the amount of energy corresponding to the annual global energy consumption, represents a crucial advance towards the development of a carbon-neutral and sustainable energy society.[1,2] Photoelectrochemical (PEC) water splitting is one of the solar energy conversion processes which has garnered growing attention as renewable route to convert and store sunlight into clean $H_2$ from a renewable source using a semiconductor/electrolyte junction.[3] Despite intense research since 1972,[4] many efforts have been devoted to the fabrication of efficient photoanodes able to speed up the kinetically slow water oxidation semi-reaction. Visible light active, stable and earth abundant photoactive materials are urgently needed for this purpose.[5]

Ternary oxides are being increasingly preferred over the largely studied binary semiconductor oxides such as $WO_3$ and $TiO_2$, because of the possibility of finely tuning the position of their valence and conduction bands, and consequently their band gap energy, by simply changing the metal cations.[6–8] $BiVO_4$ is to date the state of the art ternary oxide photoanode material thanks to its relatively long-lived charge carriers,[9] providing an internal quantum efficiency close to unity up to 450 nm,[10] although with its 2.4 eV band gap it would allow a maximum sunlight-to-hydrogen conversion efficiency of *ca.* 8% only.[11,12] Alternative ternary oxide materials providing a more effective use of visible light are very actively sought.[6,13,14]

Copper tungstate ($CuWO_4$), with a band gap of *ca.* 2.3 eV corresponding to an absorption edge of 550 nm, represents a good candidate material for PEC devices, also thanks to its good stability in PEC water oxidation under prolonged solar irradiation in neutral and slightly basic solutions and high selectivity towards the oxygen evolution reaction.[15–19] However, best-performing $CuWO_4$ electrodes produce no more than 0.4 mA $cm^{-2}$ under 1 sun illumination at 1.23 $V_{RHE}$, quite far from the theoretical limit.[20] Doping-level substitution of $Cu^{2+}$ ions with $Fe^{3+}$ or $Ni^{2+}$ was reported to increase both photocurrent generation[21] and charge separation efficiency,[22] while increased visible-light sensitised photoanodes were obtained by partial substitution of $W^{6+}$ with $Mo^{6+}$ ions in the $CuWO_4$ structure, due to a band gap energy reduction from 2.3 to 2.0 eV.[23–26] Furthermore, also the construction of heterojunctions with other photocatalysts such as $WO_3$ and $BiVO_4$ [27–30] may improve the spatial separation of photoproduced charge carriers.[31,32]

Aiming at producing robust and efficient photoanodes, in the present work we perform a systematic investigation of the PEC

[a]*Dipartimento di Chimica, Università degli Studi di Milano, Via Golgi 19, 20133 Milano, Italy. E-mail: mariavittoria.dozzi@unimi.it*

[b]*Eni S.p.A, Novara Laboratories (NOLAB), Renewable, New Energies and Material Science Research Center (DE-R&D), Via G. Fauser 4, I-28100 Novara, Italy*

[c]*Laboratory for Molecular Engineering of Optoelectronic Nanomaterials, École Polytechnique Fédérale de Lausanne (EPFL), 1015 Lausanne, Switzerland*

† Electronic supplementary information (ESI) available. See DOI: https://doi.org/10.1039/d4se00161c

performance of a series of $CuW_{1-x}Mo_xO_4$ materials with increasing Mo for W substitution ($x$ = 0–0.8). The structural properties of each obtained material have been fully characterized, with the aim of elucidating the effects that Mo for W substitution has on the structure and photoactivity of the materials and establishing a structure–photoactivity correlation for these very promising, though up to now scarcely investigated, ternary metal oxide-based semiconductor materials. A novel synthesis route was explored, which proved successful to produce transparent, *ca.* 250 nm thick photoactive layers in a single step, ensuring up to 90% light absorption at 420 nm, which perform much better than those obtained through the previously adopted multilayer approach,[24] due to minimization of charge recombination at the interface between consecutive layers. The far improved photogenerated charge separation capability of the identified best performing copper molybdo-tungstate material (with $x = 0.5$) is unequivocally demonstrated through *in operando* intensity modulated photocurrent spectroscopy analysis, which allowed us to clearly distinguish between bulk and surface processes in limiting the overall PEC performance.

Finally, we demonstrate that the superior photoactivity of the optimal $CuW_{0.5}Mo_{0.5}O_4$ photoanode material with respect to pure $CuWO_4$ can be further enhanced by coupling it with $BiVO_4$ in a never explored so far heterojunction system.

## 2. Experimental

### 2.1. Chemicals and materials

The following chemicals, all purchased from Sigma Aldrich, were employed as supplied: copper(II) nitrate trihydrate (99%, $Cu(NO_3)_2 \cdot 3H_2O$), ammonium metatungstate hydrate (99%, $(NH_4)_6H_2W_{12}O_{40} \cdot xH_2O$), citric acid (99%), boric acid (99%) and ethanol (99%), bismuth(III) nitrate pentahydrate (≥98%), ammonium metavanadate (≥99%), nitric acid 23.3%. Ammonium heptamolybdate tetrahydrate (99%, $(NH_4)_6Mo_7O_{24} \cdot 4H_2O$) was an Alfa Aesar product. Fluorine-doped 2 mm thick tin oxide (FTO) glass was purchased from Pilkington Glass (TEC-7). Ammonium metatungstate hydrate (85%, $(NH_4)_6H_2W_{12}O_{40} \cdot xH_2O$) was employed as precursor in the preliminary screening of $CuW_{1-x}Mo_xO_4$ materials with different Mo for W substitution ($x$ = 0–0.8).

### 2.2. Preparation of photoelectrodes

All investigated photoanodes were prepared *via* spin coating onto previously cleaned fluorine doped tin oxide (FTO), followed by thermal annealing.

A 1.0 M solution of $CuWO_4$ was prepared by adding 14.0 mmol of citric acid, 5.0 mmol of copper nitrate and 0.4167 mol of ammonium metatungstate to 5.0 mL of an ethanol/water solution prepared by mixing 10.6 mL of ethanol with 4.8 mL of $H_2O$. The precursors were dissolved by keeping the solution under constant stirring for 30 min at 80 °C up to complete dissolution of the metal precursor. The so-obtained blue solution is stable for several weeks.

In the preliminary study on Mo for W substitution, a 1.0 M solution of $CuW_{1-x}Mo_xO_4$ with $x = 0.20$, 0.35, 0.65 and 0.80 was prepared by adding 14.0 mmol of citric acid, 5.0 mmol of copper nitrate, 0.2083 mol of ammonium metatungstate (85% purity) and the corresponding proper amount of the ammonium heptamolybdate to 5.0 mL of the above-mentioned ethanol/water solution. The precursors were dissolved by keeping the solution under constant stirring for 30 min at 80 °C up to complete dissolution. The so-obtained green solution is stable for several weeks. Then, in all studies on optimum $CuW_{0.5}Mo_{0.5}O_4$, a 1.0 M solution was prepared by adding 0.3571 mmol of ammonium molybdate in place of the corresponding amount of ammonium metatungstate (99% purity).

A 0.3 M solution of $BiVO_4$ was prepared as reported elsewhere.[9] Typically, 2 mmol of $Bi(NO_3)_3$ and $NH_4VO_3$ were added to 6 mL of 23% $HNO_3$ containing 4 mmol of citric acid, acting as a stabilizer. The solution was kept under stirring at room temperature up to complete dissolution of all precursors.

Prior to deposition, the FTO glass was cleaned by 30 min long sonication in a soap solution, followed by careful washing, sonication in ethanol for 30 min and drying in air. The clean glass was then cut into 2.5 × 2.5 $cm^2$ slices that underwent a 15 min-long UV-cleaner ozone treatment to remove any organic species deposited onto the FTO surface. 100 μL of each precursor paste was deposited onto clean FTO, followed by spinning at 4000 rpm for 30 s with an acceleration rate of 3000 rpm $s^{-1}$. After deposition, the electrodes were annealed at 550 °C for 1 h after 1 h-long temperature ramp and then cooled down to room temperature. When electrodes consisted of a $BiVO_4$ single layer or $BiVO_4$ was an overlayer in the heterojunction system, the annealing temperature was 500 °C.

$CuW_{1-x}Mo_xO_4$ electrodes with $x$ = 0–0.8 consisted of single layer films. $CuW_{0.5}Mo_{0.5}O_4$ multilayer films were obtained by repeating the deposition procedure followed by intermediate annealing, up to 3 times. A $CuWO_4$ electrode with a film thickness comparable to that of the optimum $CuW_{0.5}Mo_{0.5}O_4$ single layer film was obtained with a 2 layers deposition followed by annealing.

The $CuW_{0.5}Mo_{0.5}O_4/BiVO_4$ heterojunction photoanode was obtained by depositing 8 $BiVO_4$ layers, corresponding to a *ca.* 150 nm thick film, onto a $CuW_{0.5}Mo_{0.5}O_4$ monolayer film, predeposited on FTO. A $BiVO_4$ film with comparable thickness was obtained by 8 layers deposition onto the FTO substrate.

The $CuW_{0.5}Mo_{0.5}O_4$ photoanodes obtained by deposition of 1, 2 or 3 layers of this material were labelled as $CuW_{0.5}Mo_{0.5}O_4$ 1L, $CuW_{0.5}Mo_{0.5}O_4$ 2L or $CuW_{0.5}Mo_{0.5}O_4$ 3L, respectively. The following other labels are employed: CuW for $CuWO_4$, CuWMo for $CuW_{0.5}Mo_{0.5}O_4$ 1L, BV for $BiVO_4$, and CuWMo/BV for the $CuW_{0.5}Mo_{0.5}O_4/BiVO_4$ heterojunction.

### 2.3. Optical, structural and morphological characterization

The absorption spectra of the materials were recorded in the transmission mode using a Jasco V-670 spectrophotometer. Their crystalline phase was investigated through X-ray diffraction (XRD) analysis using a Philips PW1820 diffractometer, equipped with a Cu sealed tube that provided Kα radiation at 40 mA and 40 kV. A model JEOL JM 7600F scanning electron microscope operating at a 10 kV accelerating voltage and at 8 mm working distance was used to acquire the top view and cross-section images.

### 2.4. Photoelectrochemical tests

PEC measurements were carried out using a three electrode cappuccino cell equipped with two quartz windows. The here synthesized photoanodes were used as working electrodes, an Ag/AgCl (3.0 M NaCl) as reference electrode and a platinum gauze as counter electrode. The electrical bias was swept using an Autolab PGSTAT 12, controlled by the NOVA software. The light source was an Oriel, Model 81172 solar simulator equipped with an AM 1.5 G filter. The light intensity, measured by means of a Thorlabs PM200 power meter equipped with a S130VC power head with Si detector, was 100 mW $cm^{-2}$. The investigated films were tested as photoanodes under both back (through the FTO side) and front (through the deposited film side) irradiation configuration, in contact with a 0.1 M $K_3BO_3$ aqueous solution at pH 9.[33] The borate buffer solution was prepared by adding KOH to aqueous boric acid up to the desired pH. A 0.1 M $NaNO_2$ aqueous solution, $K_3BO_3$ buffered at pH 9, was also employed in some linear sweep voltammetry (LSV) tests. The potential values *vs.* Ag/AgCl were converted into the RHE scale using the following equation:

$$E_{RHE} = E_{AgCl} + 0.059\ pH + E^{\circ}_{AgCl},\ \text{with}\ E^{\circ}_{AgCl}(3.0\ M\ NaCl) = 0.210\ V\ \text{at}\ 25^{\circ}C \quad (1)$$

Incident photon to current efficiency (IPCE) measurements were carried out under irradiation with a 300 W Lot-Oriel Xe lamp equipped with a Lot-Oriel Omni-λ 150 monochromator and a Thorlabs SC10 automatic shutter, in the above described three-electrode cell containing either $K_3BO_3$ only or $NaNO_2$ buffered solutions. The IPCE plots were recorded at 1.23 $V_{RHE}$ within the 350–650 nm wavelength range, with a 10 nm step. A 420 nm filter was employed at $\lambda > 500$ nm, to cut any high-order harmonics originated from the monochromator. The IPCE values were calculated as:

$$IPCE = \frac{1240 \times J}{P_\lambda \times \lambda} \times 100 \quad (2)$$

where $J$ is the photocurrent density (mA $cm^{-2}$) and $P_\lambda$ (mW $cm^{-2}$) is the power measured at each specific wavelength $\lambda$ (nm). IQE plots were obtained by normalizing the corresponding IPCE curves for the photons absorbed by the material, obtained from the absorbance ($A$) spectrum, according to:

$$IQE = \frac{IPCE(\lambda)}{1 - 10^{-A(\lambda)}} \quad (3)$$

Intensity modulated photocurrent spectroscopy (IMPS) measurements were performed using a customized blue light modulation system with 4 Cree XLamp MC-E LEDs. The Blue LED was powered at a DC background of 3.4 V with a 200 mV sinusoidal perturbation from a function generator (Tektronix AFG3021C) from 1000 kHz to 0.1 Hz. A three-electrode configuration cell was employed, similar to that employed in PEC measurements. A Thompson Electrochem potentiostat (model 251) was used to control the applied potential on the working electrode. The IMPS response was recorded by a digital oscilloscope (Tektronix DPO7254C) *via* a 50 Ω resistor (Velleman E6/E12) in series with a platinum counter electrode.

## 3. Results and discussion

### 3.1. $CuW_{1-x}Mo_xO_4$ photoelectrodes ($x$ = 0–0.8) and screening of the film thickness

A systematic analysis on all investigated $CuW_{1-x}Mo_xO_4$ materials with $x$ = 0–0.8 was first performed to identify the optimum Mo for W substitution degree, followed by the study on the film thickness of the best performing electrode. The XRD patterns of the whole series of $CuW_{1-x}Mo_xO_4$ electrodes are shown in Fig. 1. All patterns display all the reflections characteristic of pure wolframite regardless of the Mo for W substitution degree, indicating that Mo for W substitution has no effects on the crystalline phase.

Compared to the XRD pattern of pure $CuWO_4$ ($x$ = 0), a shift of the reflexes at 30.25° and 32.25° toward lower and higher 2$\theta$ values, respectively, is observed with progressively increasing Mo for W substitution (a detailed view of Fig. 1 is shown in Fig. S1 of the ESI file†), indicating the successful incorporation of Mo into the $CuWO_4$ lattice.[24,26] The characteristic wolframite peaks, well evident up to a 50% Mo for W substitution ($x$ = 0.5), become progressively less marked for higher molybdenum contents ($x$ = 0.65 and 0.80), probably due to the loss of

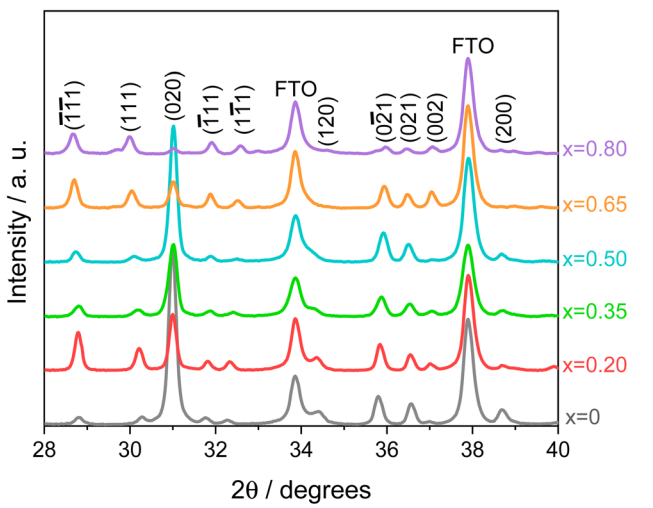


Fig. 1 XRD patterns in the 28° to 40° 2$\theta$ region of $CuW_{1-x}Mo_xO_4$ electrodes, with $x$ = 0–0.8. The characteristic Miller indices of pure $CuWO_4$ wolframite single crystal structure (JCPDF 72-0616)[34] are indicated. FTO peaks are also reported.

 

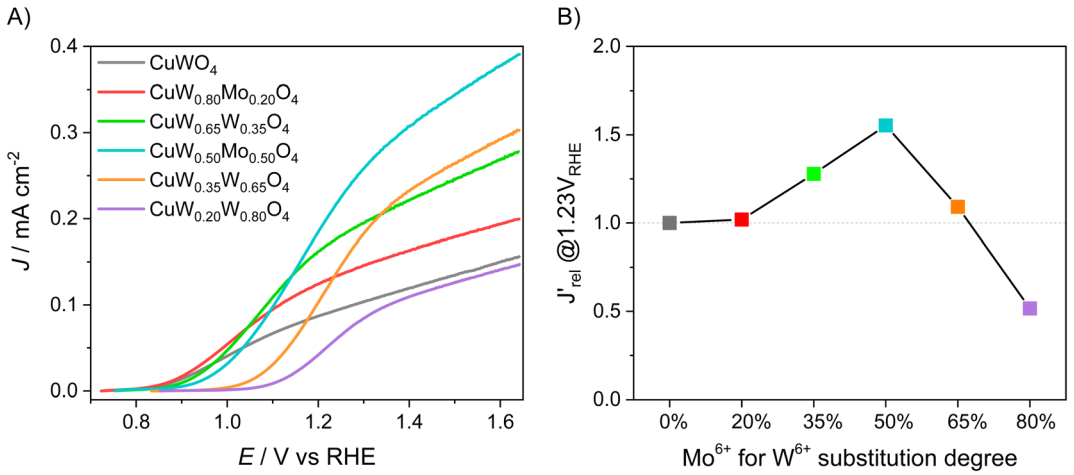


Fig. 2 (A) Linear sweep voltammetry (LSV) scans of $CuW_{1-x}Mo_xO_4$ films with different $Mo^{6+}$ for $W^{6+}$ substitution degrees, under back-side irradiation. (B) Trend of the relative photocurrent efficiency $J'_{rel}$, defined in the main text, *vs.* the percent of Mo for W substitution degree.

wolframite structure in favour of the triclinic structure typical of α-$CuMoO_4$ at room temperature,[35] or to possible $CuW_{1-x}Mo_xO_4$ partial segregation into $WO_3$ and $CuMoO_4$.[23]

The LSV scans in water photo-oxidation conditions for all investigated electrodes with different Mo for W substitution are reported in Fig. 2A. By dividing the $J$ values at 1.23 $V_{RHE}$ extracted from this figure by the maximum theoretical photocurrent density $J_{abs}$ of each photoelectrode, calculated by integrating the absorption spectrum of each photoanode (Fig. S2†) over the solar spectrum, we obtained the photocurrent efficiency values $J'$ of each photoelectrode. To have a clearer insight of the effects of Mo for W substitution, we finally calculated the $J'_{rel}$ values, reported in Fig. 2B, obtained as the ratio between the $J'$ value of each photoelectrode and the $J'$ value of pure $CuWO_4$. The best performing electrode, in terms of both absolute photocurrent density under steady state condition and photocurrent onset at relatively low potentials, corresponds to the $CuW_{0.5}Mo_{0.5}O_4$ film, obtained by 50% Mo for W substitution. In fact, Fig. 2B evidences a bell-shaped trend for the $J'_{rel}$ values for different $Mo^{6+}$ for $W^{6+}$ substitution ($x = 0$–$0.8$), with a maximum for 50% substitution, and a progressive photocurrent efficiency lowering for higher substitution degrees, with $CuW_{0.2}Mo_{0.8}O_4$ performing even worse than pure $CuWO_4$. Furthermore, a progressive shift of the photocurrent onset toward more positive potential values occurs with increasing $Mo^{6+}$ ions incorporation (Fig. 2A). The origin of this optimum compromise is in line with the best charge separation efficiency attained upon optimum 50% Mo for W incorporation (Fig. S3†).

Once assessed the optimal 50% Mo for W substitution, we investigated the effects of the photoactive layer thickness. The SEM top view and cross-section images of the optimum $CuW_{0.5}Mo_{0.5}O_4$ material as 1-layered (1L), 2-layered (2L) and 3-layered (3L) films are shown in Fig. 3. Top views (Fig. 3A–C) account for a granular, grape-like shaped morphology for the 1L

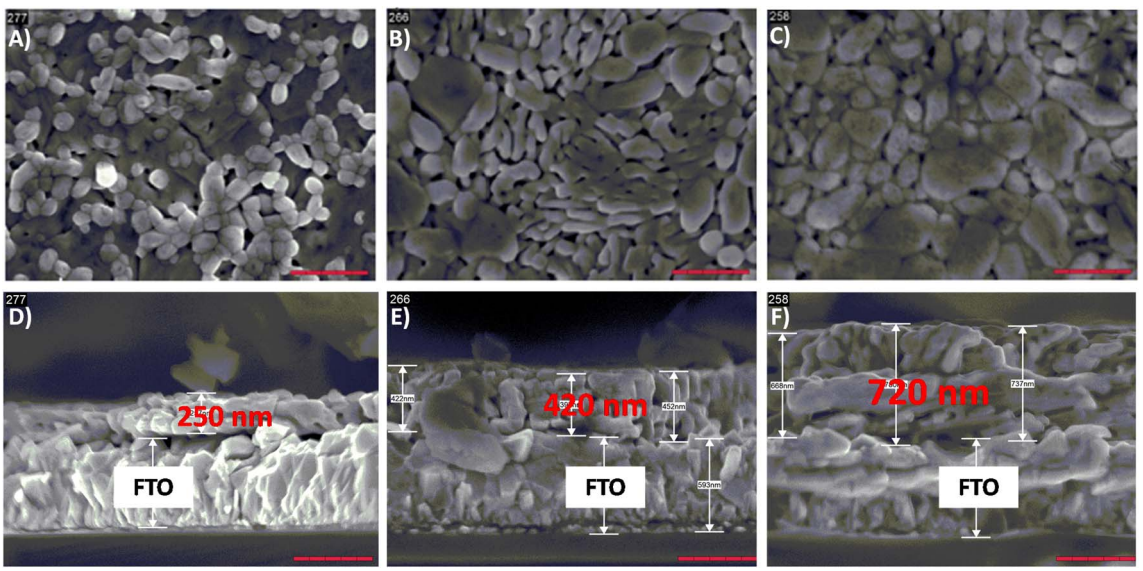


Fig. 3 (A–C) Top view and (D–F) cross section SEM images at 50$k$× magnification of (A and D) $CuW_{0.5}Mo_{0.5}O_4$ 1L, (B and E) $CuW_{0.5}Mo_{0.5}O_4$ 2L and (C and F) $CuW_{0.5}Mo_{0.5}O_4$ 3L films. The scale bar is 500 nm.

Table 1 Thickness of the $CuW_{0.5}Mo_{0.5}O_4$ layers as average value obtained from Fig. 3D–F

| Sample | Thickness/nm |
|---|---|
| 1L | 250 ± 30 |
| 2L | 420 ± 40 |
| 3L | 720 ± 60 |

electrode that changes into a more compact and planar structure with increasing number of layers. This can be ascribed to the different particles packing degree consequent to the different number of annealing cycles required for the synthesis of multilayer electrodes (Table 1).

From the calculation of the absorption coefficient ($\alpha$) of the material at 420 nm, $\alpha = 7 \times 10^3$ nm$^{-1}$, and the relative absorption depth ($\delta$, see Table S1†), the thinnest, *ca.* 250 nm thick, 1L film was found to be already able to absorb *ca.* 90% of the 420 nm incident radiation. Moreover, both LSV and IPCE analyses on $CuW_{0.5}Mo_{0.5}O_4$ electrodes within the 250–720 nm thickness range (see Fig. S5†) account for the 250 nm thick photoactive layer (1L film) as the best performing one thanks to an optimum compromise between light absorption and charge separation efficiency.

Interestingly, the *ca.* 250 nm thick monolayer CuWMo electrode, obtained with 50% Mo for W substitution in the present study performs much better than the similarly thick $CuW_{0.5}Mo_{0.5}O_4$ electrode prepared through a multilayer procedure,[24] in terms of both higher *J–V* curve fill factor over the whole investigated potential range and photocurrent density at the 1.23 $V_{RHE}$ reference potential. Indeed, the lower number of depositions (each followed by annealing) ensures a lower number of interfaces, which may act as recombination centres. Furthermore, a better optical transparency allows for a more efficient use of the absorbed light.

Table 2 Atomic percent composition of CuW and CuWMo electrodes, from EDX analysis

| | Atom% | |
|---|---|---|
| | CuW | CuWMo |
| Cu | 50.72 | 50.31 |
| W | 49.28 | 24.40 |
| Mo | — | 25.39 |

### 3.2. PEC performance of $CuW_{0.5}Mo_{0.5}O_4$ (CuWMo) *vs.* $CuWO_4$ (CuW) photoelectrodes

The effective Mo for W substitution in $CuW_{0.5}Mo_{0.5}O_4$ was proven by the energy-dispersive X-ray spectroscopy (EDX) mapping analyses reported in Table 2, accounting for a *ca.* equal co-presence of W and Mo in CuWMo.

The SEM top view images of the CuW and CuWMo electrodes evidence a grape-like shaped morphology for both films (Fig. S6A and B†), with the molybdenum-containing material exhibiting a less compact structure, possibly facilitating the electrolyte/film contact across the whole film thickness. The cross-section images reported for the CuW (Fig. S6C†) and CuWMo (Fig. S6D†) electrodes account for a comparably thick photoactive layer of $CuWO_4$ and $CuW_{0.5}Mo_{0.5}O_4$ electrodes. The absorption spectra of CuW and CuWMo (Fig. S6E†) confirm a comparable thickness for these two electrodes, without any significant light scattering or absorption onset variation upon 50% $Mo^{6+}$ for $W^{6+}$ substitution.

The LSV and the IQE curves obtained with CuWMo in both back- and front-irradiation configurations are shown in Fig. 4 in comparison with those obtained with the CuW electrode. Upon 50% Mo for W substitution in $CuWO_4$, a 6-fold enhancement in photocurrent production at 1.6 $V_{RHE}$ is attained (Fig. 4A) and a far higher photoactivity, extending to the visible region up to above 550 nm, as evidenced by the IQE plots in Fig. 4B. This confirms a far extended visible light exploitation. Moreover, the higher performance in front- with respect to back-side irradiation accounts for hole transport across the material bulk as more limiting than electron transport.

The charge injection and charge separation efficiency, $\eta_{inj}$ and $\eta_{sep}$, respectively, of the CuW and CuWMo electrodes,

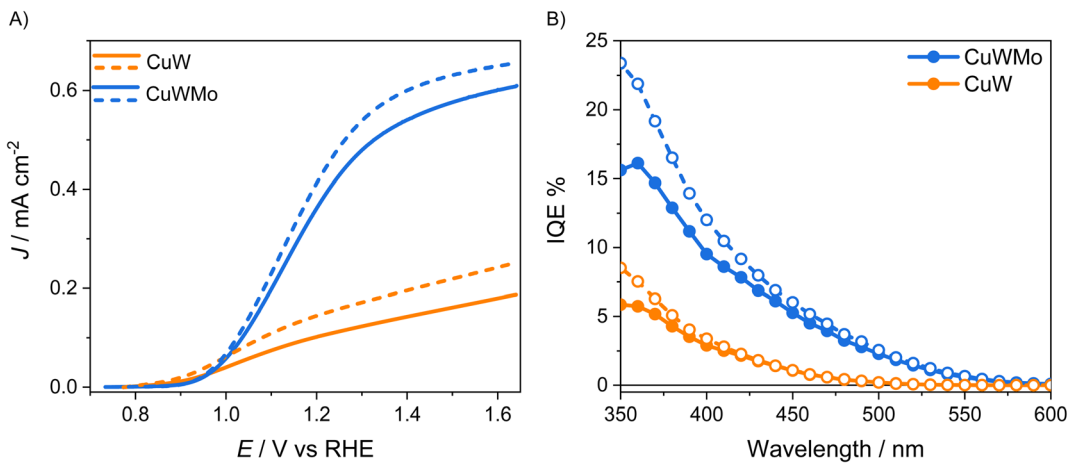


Fig. 4 (A) Linear sweep voltammetry (LSV) and (B) internal quantum efficiency (IQE) curves at 1.23 $V_{RHE}$ of the CuWMo (blue) and CuW (orange lines) electrodes with comparable film thickness, in 0.1 M $K_3BO_3$, under back- (solid lines, full circles) and front-side irradiation (dashed lines, void circles).

 

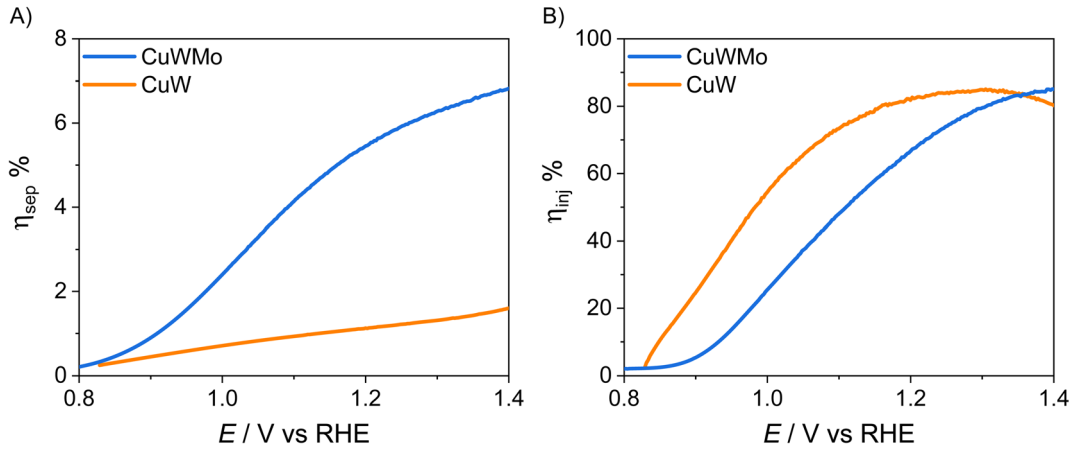


Fig. 5 (A) Charge injection, $\eta_{inj}$, and (B) charge separation efficiency, $\eta_{sep}$, of CuWMo (blue) and CuW (orange) films *vs.* applied potential, under back-side irradiation.

calculated from LSV plots in the presence and absence of the $NaNO_2$ hole scavenger as detailed in the ESI file,† are reported in Fig. 5, as a function of the applied potential. The $\eta_{inj}$ and $\eta_{sep}$ values of CuWMo at 1.23 $V_{RHE}$ are 52% and 6%, respectively, which point to charge separation in the material bulk as the main limiting factor for this material. Even lower is $\eta_{sep}$ for CuW under the same conditions, which once again confirms the extremely low charge separation efficiency as main limitation of the PEC performance of copper tungstate.

As shown in Fig. 5A, Mo for W substitution is beneficial over the whole investigated potential range, resulting in an almost 6-fold higher bulk charge separation at 1.23 $V_{RHE}$, with a parallel modest decrease in surface charge injection efficiency (Fig. 5B). This is in line with the relative shift in photocurrent onset towards more positive potential values observed in LSV plots and tentatively attributed to additional trap surface states introduced in $CuWO_4$ by Mo for W substitution.[15–17,33,36]

However, the $\eta_{sep}$ and $\eta_{inj}$ values estimated from measurements in the presence of sacrificial reagents may not be representative for water oxidation, especially under sluggish oxidation conditions, *i.e.*, in the presence of a significant charge accumulation at the semiconductor–liquid junction. In fact, sacrificial redox agents involved in the electrochemical reaction at the film/electrolyte interface can affect band bending and charge accumulation, depending on their nature.[37]

On the other hand, intensity modulated photocurrent spectroscopy (IMPS) is a powerful tool in the frequency domain, which allows to unequivocally decouple the bulk and surface contributions of photoanodes by their respective time constants *in operando*, *i.e.*, with the electrodes in contact with a buffered solution without any sacrificial species.[38,39] Thus, a more accurate evaluation of $\eta_{sep}$ and $\eta_{inj}$ for the CuW and CuWMo electrodes was obtained through IMPS measurements in 0.1 M $K_3BO_3$ electrolyte solution. The IMPS response for the CuWMo and CuW films are shown in Fig. 6A as Nyquist plots of the complex photocurrent, at 1.6 $V_{RHE}$.

All Nyquist plots are typically composed of two semicircles, *i.e.*, the negative semicircle located in the lower quadrant and representative of charge transport in the bulk (higher frequency process) and the positive semicircle located in the upper quadrant and associated with surface recombination (lower frequencies process).[40] Notably, in all cases the surface recombination semicircle is significantly smaller than the bulk transport, indicating that a large steady state photocurrent is

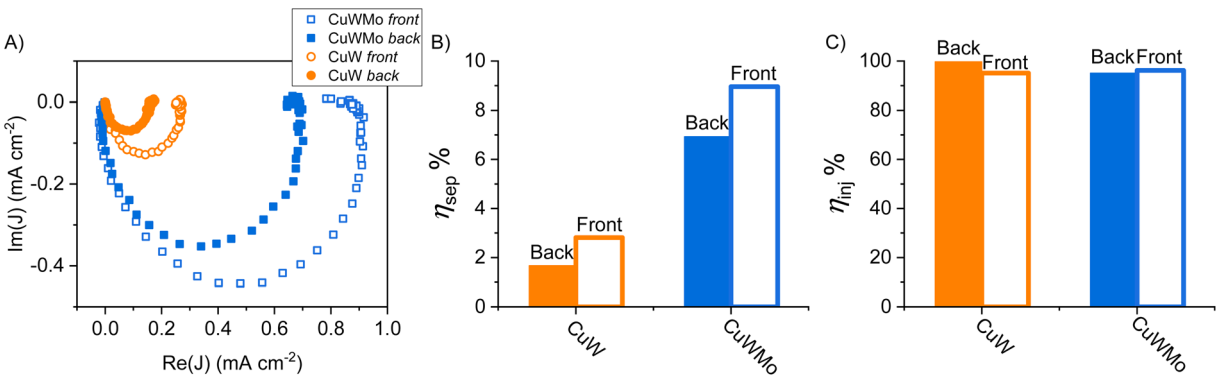


Fig. 6 (A) IMPS analyses at 1.6 $V_{RHE}$ for CuWMo (blue) and CuW (orange) electrodes in 0.1 M $K_3BO_3$ under back- (full symbols) and front-side (void symbols) irradiation. The represented raw data were obtained upon normalization to the electron current recorded using the IMPS setup. (B) Charge separation ($\eta_{sep}$) and (C) charge injection ($\eta_{inj}$) efficiencies calculated from IMPS data under back- (filled columns) and front-side (void columns) irradiation.

available for water oxidation at the photoanodes surface, as with other n-type metal oxides.[41–43]

The $\eta_{sep}$ and $\eta_{inj}$ values calculated *in operando* (see Section S3 in the ESI†) for each investigated electrode, under front- or back-side irradiation at 1.6 $V_{RHE}$ are reported as histograms in Fig. 6B and C. The far better bulk charge transport properties of the optimized CuWMo photoanode compared to the pure CuW electrode are confirmed by the more than 4-fold higher $\eta_{sep}$ in both irradiation configurations (Fig. 6B), with no significant change in the $\eta_{inj}$ of the original material (Fig. 6C). Noteworthy, far higher bulk electron transport compared to bulk hole transport is evidenced by the larger $\eta_{sep}$ value obtained in front-rather than back-side irradiation, in line with the PEC performances presented in Fig. 4. IMPS results are in full agreement with those obtained in the presence of the $NaNO_2$ hole scavenger (Fig. 5) and unequivocally demonstrate that the superior charge separation is the main origin of the far higher PEC performance of CuMoW with respect to CuW. This unequivocally attained $\eta_{sep}$ increase is most likely related to the increased majority carrier concentration in 0.5% Mo-substituted $CuWO_4$ with respect to pure $CuWO_4$, with a consequent improved material conductivity also evidenced by Mott–Schottky analyses reported in previous studies for similar systems.[23,25,26]

### 3.3. The $CuW_{0.5}Mo_{0.5}O_4/BiVO_4$ heterojunction system

Aiming at exploiting possible synergies between $CuW_{0.5}Mo_{0.5}O_4$, absorbing up to 550 nm, and $BiVO_4$, having a 2.4 eV bandgap,[9] an excellent conversion efficiency up to *ca.* 520 nm and a pronounced absorption shoulder in the 400–480 nm visible region (see absorption spectra in Fig. S6E†), we deposited a $BiVO_4$ layer on top of the CuWMo electrode. The presence of the characteristic signals of monoclinic $BiVO_4$ in the XRD pattern of the so obtained composite electrode (Fig. S7†), together with the same set of XRD peaks observed with CuWMo monolayer films, confirm the successful formation of the CuWMo/BV heterojunction. The presence of the $BiVO_4$ overlayer on top of the CuWMo film induces a substantial absorption increase in the visible range up to 480 nm, particularly around 420 nm, where the absorption feature typical of $BiVO_4$ is centred (Fig. S6E†). The top view morphology of the films significantly changes upon $BiVO_4$ deposition (Fig. S8A†), switching from the granular grape-like shape observed for CuWMo (Fig. S6B†) to a more compact and planar structure, consequent to the deposition of successive $BiVO_4$ layers and subsequent thermal cycles. The cross-section image relative to the CuWMo/BV heterojunction electrode (Fig. S8B†) does not allow an evaluation of the effective $BiVO_4$ thickness due to the possible intercalation of the precursor solution throughout the porosity of the CuWMo underlayer, evidenced by the surface morphology change. From the increased absorption of the heterojunction at 420 nm upon $BiVO_4$ deposition and the extinction coefficient of this latter,[9] the BV overlayer was estimated to be *ca.* 170 nm thick.

The LSV and IQE plots recorded with the CuWMo, CuWMo/BV and single BV electrodes under back- and front-side irradiation can be compared in Fig. 7 and 8, respectively.

As shown in Fig. 7A, under back-side irradiation the heterojunction system exhibits a slight LSV performance improvement in comparison to single CuWMo and BV, while under front-side irradiation the photoactivity enhancement is much larger (Fig. 7B). Moreover, BV deposition induces an appreciable earlier photocurrent onset in the *J–V* curves at lower applied potentials compared to that of the CuWMo single material, in line with the far energetically higher $BiVO_4$ CB[44] with respect to that of $CuWO_4$-based materials.[15,45,46]

The IQE results at 1.23 $V_{RHE}$ (Fig. 8) evidence that any visible light photoactivity gain achieved upon coupling CuWMo with BV strongly depends on the irradiation configuration, which in turn implies the wavelength-dependent selective photoexcitation of one oxide, or rather the simultaneous excitation of the two coupled oxides in the heterojunction.[47,48] Indeed, higher conversion efficiencies were selectively obtained with the heterojunction under front-rather than back-side irradiation

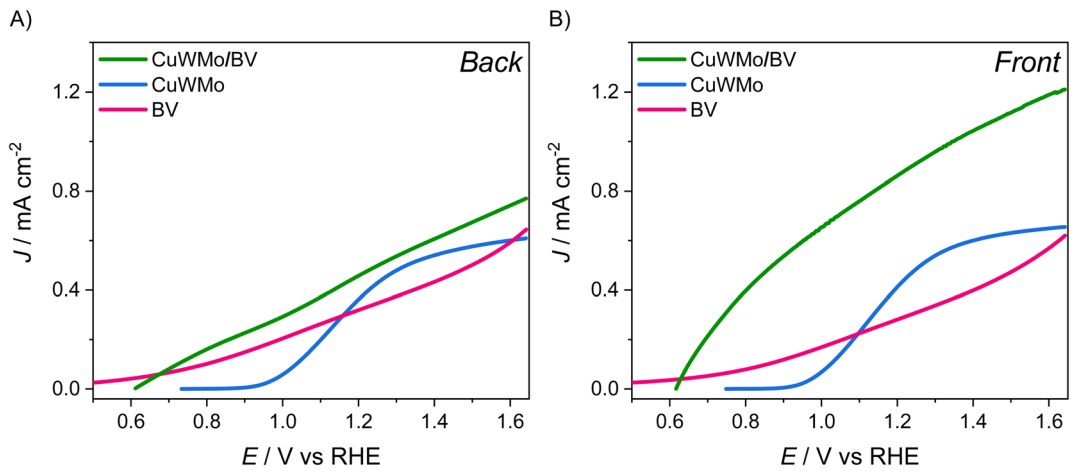


Fig. 7 Linear sweep voltammetry (LSV) scans recorded with CuWMo (blue), BV (magenta) and CuWMo/BV electrode (green) under (A) back-side and (B) front-side irradiation.

 

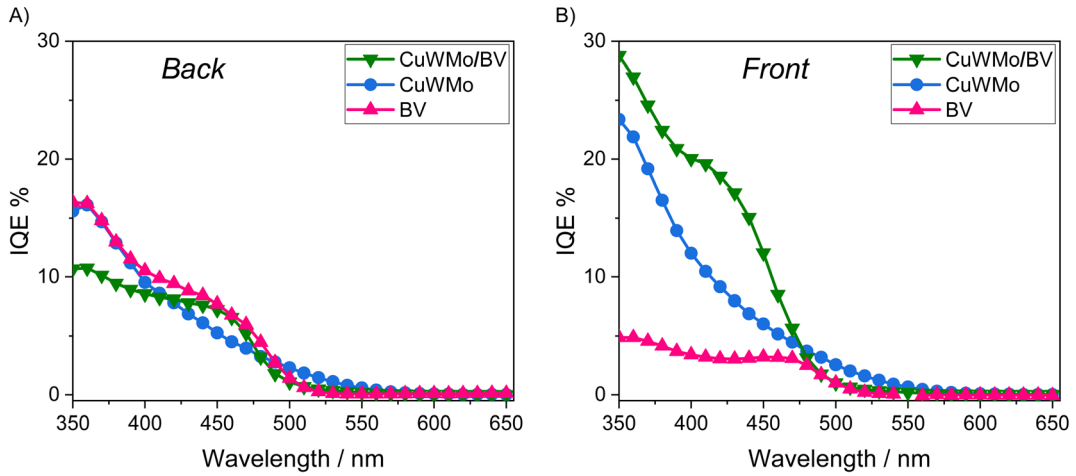


Fig. 8 IQE plots recorded at 1.23 $V_{RHE}$ with the CuWMo (blue), BV (magenta) and CuWMo/BV (green) electrodes under (A) back-side and (B) front-side irradiation.

(Fig. 8A *vs.* 8B) and a strong dependence on the excitation wavelength is also outlined.

The peculiar behavior attained with the heterojunction system compared to the corresponding single oxide under the two irradiation configurations can be best envisaged in terms of the IQE enhancement factor reported in Fig. 9, and calculated according to the following equation:[49]

$$IQE_{enhancement} = IQE_{CuWMo/BV} - (IQE_{CuWMo} + IQE_{BV}) \quad (4)$$

where $IQE_{CuWMo/BV}$ is the IQE measured with the coupled system, while $IQE_{CuWMo}$ and $IQE_{BV}$ are the IQEs of the CuWMo and BV photoanodes recorded in separate experiments, respectively.

Under back-side irradiation the IQE enhancement factor is negative over the entire wavelength region. This indicates the lack of any synergism upon coupling the two oxides when CuWMo is excited first, so that a large portion of electron–hole couples, accounting for at least a 90% absorption of the radiation, are generated within CuWMo. The overall photoactivity decrease exhibited by the composite material, especially at $\lambda <$ 400 nm where the incident light firstly excites the inner CuWMo layer, or at $\lambda >$ 480 nm with photons selectively absorbed by the CuWMo compart, can be related to inefficient hole transfer from CuMoW through the BV overlayer. In the 400 < $\lambda$ < 480 nm range, *i.e.*, upon simultaneous excitation of both oxides, a charge recombination pathway at the interface of the two oxides may also occur, as already evidenced for $WO_3$/$BiVO_4$ heterojunctions.[47,49,50]

On the other hand, the IQE enhancement factor exhibits a different trend under front-side irradiation (Fig. 9). In particular, the negative IQE enhancement factor in the wavelength region where BV does not strongly absorb ($\lambda >$ 480 nm) evidences that the selective excitation of the inner CuWMo layer in the composite is not followed by any effective hole transfer toward the electrolyte through the BV overlayer (Fig. 10A). This confirms the inability of CuWMo to sensitise BV in the longer wavelength region, as also observed under back-side irradiation (Fig. 9).

On the other hand, at $\lambda <$ 480 nm, where BV is the main absorbing layer, the IQE enhancement factor under front-side irradiation tends to become positive (Fig. 9), and it is no more superimposed to that observed under back-side irradiation. The charge carriers photogenerated in BV may fully exploit the staggered band edge alignment at the interface between the two oxides, with a consequent more efficient charge separation across the composite system (Fig. 10B), determining a maximum IQE enhancement factor value at *ca.* 420 nm, where BV exhibits its highest absorption and photoactivity. This positive synergism, guaranteed by the correct type II band alignment established at the interface of the two coupled oxides, results in the most significant gain in performance achieved upon semiconductors coupling in this configuration.

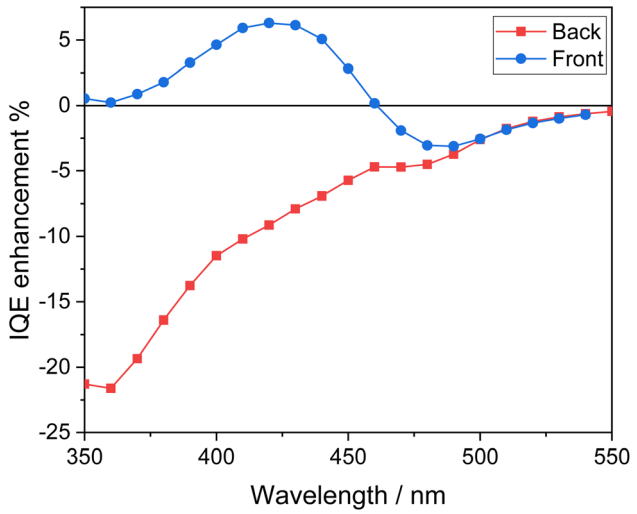


Fig. 9 IQE enhancement factor calculated from the IQE data for the CuWMo/BV coupled electrode with respect to both single CuWMo and BV components.

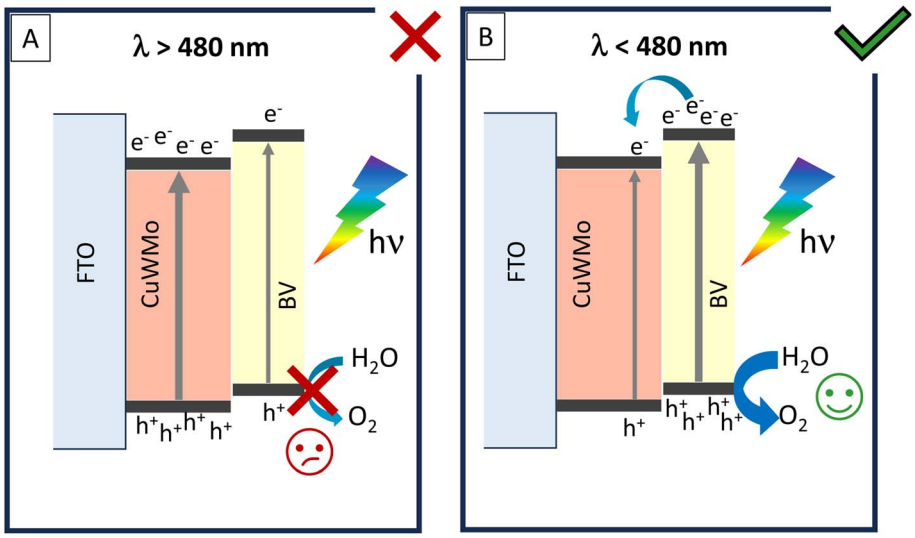


Fig. 10 Photoactivation processes in the CuWMo/BV heterojunction under front-side irradiation at wavelengths (A) above 480 nm and (B) below 480 nm.

## 4. Conclusions

A 250 nm-thick $CuW_{0.5}Mo_{0.5}O_4$ photoanode material with 50% Mo for W substitution, prepared through an effective one step deposition method, has been identified as optimal PEC performing in terms of both dopant content and film thickness.

Intensity modulated photocurrent spectroscopy (IMPS) analysis demonstrated that the superior PEC performance of $CuW_{0.5}Mo_{0.5}O_4$ results from a more efficient separation of photoproduced charges with respect to $CuWO_4$.

Coupling the $CuW_{0.5}Mo_{0.5}O_4$ photoanode with $BiVO_4$ in a heterojunction allowed for a synergistic charge separation improvement in the 350–480 nm visible range under front-side irradiation, where $BiVO_4$ behaves as main light photoabsorbing layer and has maximum photoactivity. This does not occur under back-side irradiation, when CuWMo first gets excited, because the coupled system is unable to efficiently transfer holes through the unexcited $BiVO_4$ layer.

This work demonstrates that the combination of different modification strategies can be effectively exploited to enhance the relatively low PEC performance of the extremely stable, but poorly investigated, $CuWO_4$ system.

## Data availability

All data generated or analyzed during this study are included in this published article and its ESI files.†

## Conflicts of interest

There are no conflicts to declare.

## Acknowledgements

The collaboration of Dr Marco Bompieri in performing photo(electro)catalytic experiments is gratefully acknowledged. This work was supported by the Cariplo Foundation 2021-0664 Project entitled “Carbon dioxide conversion into energy-rich molecules with tailored catalysts” (CO2EnRich) and received partial financial support from MUR (Italy), through the PRIN MAPEC (No. 2022599NR3) and PRIN CHARM (No. 20227TKTMY) projects.

## References

1 N. S. Lewis and D. G. Nocera, *Proc. Natl. Acad. Sci. U. S. A.*, 2006, **103**, 15729–15735.
2 N. S. Lewis, *Science*, 2016, **351**, 6271.
3 M. Grätzel, *Nature*, 2001, **414**, 338–344.
4 A. Fujishima and K. Honda, *Nature*, 1972, **238**, 37–38.
5 K. Sivula and R. van de Krol, *Nat. Rev. Mater.*, 2016, **1**, 15010.
6 D. K. Lee, D. Lee, M. A. Lumley and K.-S. Choi, *Chem. Soc. Rev.*, 2019, **48**, 2126–2157.
7 Y. Tang, N. Rong, F. Liu, M. Chu, H. Dong, Y. Zhang and P. Xiao, *Appl. Surf. Sci.*, 2016, **361**, 133–140.
8 L. A. Cipriano, G. Di Liberto, S. Tosoni and G. Pacchioni, *J. Chem. Theory Comput.*, 2020, **16**, 3786–3798.
9 A. Polo, M. V. Dozzi, I. Grigioni, C. Lhermitte, N. Plainpan, L. Moretti, G. Cerullo, K. Sivula and E. Selli, *Sol. RRL*, 2022, **6**, 2200349.
10 M. Tayebi and B. K. Lee, *Renewable Sustainable Energy Rev.*, 2019, **111**, 332–343.
11 J. H. Kim, J.-W. Jang, Y. H. Jo, F. F. Abdi, Y. H. Lee, R. van de Krol and J. S. Lee, *Nat. Commun.*, 2016, **7**, 13380.
12 S. Wang, P. Chen, Y. Bai, J.-H. Yun, G. Liu and L. Wang, *Adv. Mater.*, 2018, **30**, 1800486.
13 L. Chen, W. Li, W. Qiu, G. He, K. Wang, Y. Liu, Q. Wu and J. Li, *ACS Appl. Mater. Interfaces*, 2022, **14**, 47737–47746.
14 S. Farhoosh, B. Eftekharinia, M. Tayebi, B. K. Lee and N. Naseri, *Appl. Surf. Sci.*, 2021, **550**, 149374.
15 C. R. Lhermitte and B. M. Bartlett, *Acc. Chem. Res.*, 2016, **49**, 1121–1129.

16 J. E. Yourey, K. J. Pyper, J. B. Kurtz and B. M. Bartlett, *J. Phys. Chem. C*, 2013, **117**, 8708–8718.
17 Y. Gao and T. W. Hamann, *J. Phys. Chem. Lett.*, 2017, **8**, 2700–2704.
18 W. Ye, F. Chen, F. Zhao, N. Han and Y. Li, *ACS Appl. Mater. Interfaces*, 2016, **8**, 9211–9217.
19 I. Grigioni, A. Polo, C. Nomellini, L. Vigni, A. Poma, M. V. Dozzi and E. Selli, *ACS Appl. Energy Mater.*, 2023, **6**, 10020–10029.
20 C. M. Tian, M. Jiang, D. Tang, L. Qiao, H. Y. Xiao, F. E. Oropeza, J. P. Hofmann, E. J. M. Hensen, A. Tadich, W. Li, D. C. Qi and K. H. L. Zhang, *J. Mater. Chem. A*, 2019, **7**, 11895–11907.
21 C. Nomellini, A. Polo, I. Grigioni, G. Marra, M. V. Dozzi and E. Selli, *Photochem. Photobiol. Sci.*, 2023, **22**, 2759–2768.
22 D. Bohra and W. A. Smith, *Phys. Chem. Chem. Phys.*, 2015, **17**, 9857–9866.
23 J. C. Hill, Y. Ping, G. A. Galli and K.-S. Choi, *Energy Environ. Sci.*, 2013, **6**, 2440–2446.
24 A. Polo, C. Nomellini, I. Grigioni, M. V. Dozzi and E. Selli, *ACS Appl. Energy Mater.*, 2020, **3**, 6956–6964.
25 J. Yang, C. Li and P. Diao, *Electrochim. Acta*, 2019, **308**, 195–205.
26 Q. Liang, Y. Guo, N. Zhang, Q. Qian, Y. Hu, J. Hu, Z. Li and Z. Zou, *Sci. China Mater.*, 2018, **61**, 1297–1304.
27 D. Wang, P. Bassi, H. Qi, X. Zhao, Gurudayal, L. Wong, R. Xu, T. Sritharan and Z. Chen, *Materials*, 2016, **9**, 348.
28 S. K. Pilli, T. G. Deutsch, T. E. Furtak, L. D. Brown, J. A. Turner and A. M. Herring, *Phys. Chem. Chem. Phys.*, 2013, **15**, 3273–3278.
29 I. Rodríguez-Gutiérrez, E. Djatoubai, M. Rodríguez-Pérez, J. Su, G. Rodríguez-Gattorno, L. Vayssieres and G. Oskam, *Electrochim. Acta*, 2019, **308**, 317–327.
30 F. Zhan, J. Li, W. Li, Y. Liu, R. Xie, Y. Yang, Y. Li and Q. Chen, *Int. J. Hydrogen Energy*, 2015, **40**, 6512–6520.
31 S. Selim, L. Francàs, M. García-Tecedor, S. Corby, C. Blackman, S. Gimenez, J. R. Durrant and A. Kafizas, *Chem. Sci.*, 2019, **10**, 2643–2652.
32 A. Polo, I. Grigioni, M. V. Dozzi and E. Selli, *Catal. Today*, 2020, **340**, 19–25.
33 K. J. Pyper, J. E. Yourey and B. M. Bartlett, *J. Phys. Chem. C*, 2013, **117**, 24726–24732.
34 J. E. Yourey and B. M. Bartlett, *J. Mater. Chem.*, 2011, **21**, 7651–7660.
35 S. C. Abrahams, J. L. Bernstein and P. B. Jamieson, *J. Chem. Phys.*, 1968, **48**, 2619–2629.
36 Y. Gao and T. W. Hamann, *Chem. Commun.*, 2017, **53**, 1285–1288.
37 D. Klotz, D. A. Grave and A. Rothschild, *Phys. Chem. Chem. Phys.*, 2017, **19**, 20383–20392.
38 E. A. Ponomarev and L. M. Peter, *J. Electroanal. Chem.*, 1995, **396**, 219–226.
39 D. Klotz, D. S. Ellis, H. Dotan and A. Rothschild, *Phys. Chem. Chem. Phys.*, 2016, **18**, 23438–23457.
40 F. Boudoire, Y. Liu, F. Le Formal, N. Guijarro, C. R. Lhermitte and K. Sivula, *J. Phys. Chem. C*, 2021, **125**, 10883–10890.
41 Y. Liu, F. Le Formal, F. Boudoire, L. Yao, K. Sivula and N. Guijarro, *J. Mater. Chem. A*, 2019, **7**, 1669–1677.
42 Y. Liu, F. Le Formal, F. Boudoire and N. Guijarro, *ACS Appl. Energy Mater.*, 2019, **2**, 6825–6833.
43 A. Polo, F. Boudoire, C. R. Lhermitte, Y. Liu, N. Guijarro, M. V. Dozzi, E. Selli and K. Sivula, *J. Mater. Chem. A*, 2021, **9**, 27736–27747.
44 J. K. Cooper, S. Gul, F. M. Toma, L. Chen, P. A. Glans, J. Guo, J. W. Ager, J. Yano and I. D. Sharp, *Chem. Mater.*, 2014, **26**, 5365–5373.
45 I. Grigioni, A. Polo, M. V. Dozzi, L. Ganzer, B. Bozzini, G. Cerullo and E. Selli, *J. Phys. Chem. C*, 2021, **125**, 5692–5699.
46 H. V. Thang, E. Albanese and G. Pacchioni, *J. Phys.: Condens.Matter*, 2019, **31**, 145503.
47 I. Grigioni, K. G. Stamplecoskie, D. H. Jara, M. V. Dozzi, A. Oriana, G. Cerullo, P. V. Kamat and E. Selli, *ACS Energy Lett.*, 2017, **2**, 1362–1367.
48 I. Grigioni, M. Abdellah, A. Corti, M. V. Dozzi, L. Hammarström and E. Selli, *J. Am. Chem. Soc.*, 2018, **140**, 14042–14045.
49 I. Grigioni, M. V. Dozzi and E. Selli, *J. Phys.: Condens.Matter*, 2020, **32**, 014001.
50 I. Grigioni, A. Polo, M. V. Dozzi, K. G. Stamplecoskie, D. H. Jara, P. V. Kamat and E. Selli, *ACS Appl. Energy Mater.*, 2022, **5**, 13142–13148.